Chemical-potential-based lattice Boltzmann method for nonideal fluids

Binghai Wen,[1,2] Xuan Zhou,[1] Bing He,[1] Chaoying Zhang,[1,*] and Haiping Fang[2]

[1]*Guangxi Key Lab of Multi-source Information Mining & Security, Guangxi Normal University, Guilin 541004, China*

[2]*Division of Interfacial Water and Key Laboratory of Interfacial Physics and Technology, Shanghai Institute of Applied Physics, Chinese Academy of Sciences, Shanghai 201800, China*

(Received 17 January 2017; revised manuscript received 27 April 2017; published 13 June 2017)

Chemical potential, as an important thermodynamic quantity, has been popularly used in thermodynamic modeling for complex systems, especially for those involving the phase transitions and chemical reactions. Here we present a chemical-potential-based multiphase lattice Boltzmann model, in which the nonideal force is directly evaluated by a chemical potential. The numerical computation is more efficient than the pressure-tensor-based model [Wen *et al.* Europhys. Lett. **112**, 44002 (2015)] because the calculations of the pressure tensor and its divergence are avoided. We have derived several chemical potentials of the popular equations of state from the free-energy density function. The theoretical analyses and numerical results support that the present model satisfies thermodynamics and Galilean invariance. An effective chemical-potential boundary condition is also implemented to investigate the wettability of a solid surface, and the contact angle can be linearly tuned by the surface chemical potential.

DOI: 10.1103/PhysRevE.95.063305

I. INTRODUCTION

Numerical simulation of multiphase flow is one of the most successful applications of the lattice Boltzmann method (LBM) [1–4]. Originating from the cellular automaton concept and kinetic theory, the intrinsic mesoscopic properties make LBM outstanding in modeling complex fluid systems involving interfacial dynamics [5–7] and phase transitions [3,4]. Shan and Chen proposed the widely used pseudopotential lattice Boltzmann method, in which the intermolecular force is mimicked by a density-dependent interparticle potential [8]. Theoretical analyses showed that its mechanical stability solution agrees with thermodynamics only if the effective mass takes the strict functional form $\psi(\boldsymbol{x}) = \psi_0 \exp(-\rho/\rho_0)$, where ρ is the density, and ρ_0 and ψ_0 are the reference density and effective mass, respectively [8,9]. This leads to the deviations between the numerical two-phase coexistence densities and the predictions from the Maxwell equal-area construction [10–12]. Recently, Li *et al.* [11] proposed an improved forcing term scheme and Khajepor *et al.* [13] proposed a multipseudopotential interaction to achieve thermodynamic consistency. The additional fitting procedures are necessary in both schemes to adapt to a specific equation of state (EOS) [3]. The Shan-Chen model was also improved for simulations with large density ratio and high stability [14,15]. Swift *et al.* proposed another popular multiphase model, which is based on free energy and incorporates a nonideal thermodynamic pressure tensor into the second equilibrium moment [16]. Inamuro *et al.* used an asymptotic analysis to accommodate the lack of Galilean invariance and extended the model to simulate multiphase flows with large density ratio [17,18]. Zheng *et al.* [19] correctly recovered the Cahn-Hilliard equation to capture the phase interface and Shao *et al.* further considered the effect of local density variation in the momentum equation [20]. Wang *et al.* proposed a multiphase lattice Boltzmann flux solver for incompressible multiphase flows with large density ratio and high Reynolds number [21,22]. Typically, these models use two kinds of distribution functions, one evolves the pressure and velocity field by the standard lattice Boltzmann equation and the other captures the phase interface by the Cahn-Hilliard equation. Recently, Wen *et al.* directly computed the nonideal force from the free energy and proposed a pressure-tensor-based multiphase flow model, which satisfies thermodynamics and Galilean invariance [12]. A similar nonideal force evaluation was also used in the entropic lattice Boltzmann method [23].

Chemical potential (CP) is the partial molar Gibbs free energy at constant pressure [24]. As an important thermodynamic quantity, it has been popularly used in thermodynamic modeling for complex systems, especially for those involving the phase transitions and chemical reactions. Some studies of multiphase flows used the chemical potential to present the phase equilibrium condition and obtain the density profile along the interfacial normal direction when the bulk free energy density takes the simplest double-well form [19,24,25]. However, both the Onsager and Stefan-Maxwell formulations of irreversible thermodynamics recognize that the chemical potential gradient is the driving force for isothermal mass transport [26,27]. Movement of molecules from higher chemical potential to lower chemical potential is accompanied by a release of free energy, and at the minimum free energy, the chemical equilibrium or the phase equilibrium is achieved. Therefore, the chemical potential plays an important role in driving a phase transition or indicating surface wettability.

In this paper, we present a multiphase lattice Boltzmann model by introducing a chemical potential to directly evaluate the nonideal force. The computational efficiency is improved since the calculation of the pressure tensor and its divergence are avoided. We also implement a chemical-potential boundary condition to effectively investigate the surface wettability and find that the contact angle is almost linear tunable by the chemical potential of the solid surface.

*zhangcy@gxnu.edu.cn

II. THEORY AND MODEL

Considering a nonideal fluid system, the free-energy functional within a gradient-squared approximation is [12,16,28]

$$\Psi = \int \left[\psi(\rho) + \frac{\kappa}{2}|\nabla\rho|^2\right] d\boldsymbol{x}, \tag{1}$$

where the first term is the bulk free-energy density at a given temperature with the density ρ and the second term gives the free-energy contribution from density gradients in an inhomogeneous system. The free energy function in turn determines the diagonal term of the pressure tensor,

$$p(\boldsymbol{x}) = p_0 - \kappa\rho\nabla^2\rho - \frac{\kappa}{2}|\nabla\rho|^2, \tag{2}$$

with the general expression of equation of state

$$p_0 = \rho\psi'(\rho) - \psi(\rho). \tag{3}$$

The full pressure tensor can be written as

$$P_{\alpha\beta}(\boldsymbol{x}) = p(\boldsymbol{x})\delta_{\alpha\beta} + \kappa\frac{\partial\rho}{\partial x_\alpha}\frac{\partial\rho}{\partial x_\beta}. \tag{4}$$

where $\delta_{\alpha\beta}$ is the Kronecker delta function. The excess pressure, namely, the nonideal force, with respect to the ideal-gas expression can be directly computed [9,12],

$$\boldsymbol{F}(\boldsymbol{x}) = -\nabla\cdot\overleftrightarrow{\boldsymbol{P}}(\boldsymbol{x}) + \nabla\cdot\overleftrightarrow{\boldsymbol{P}}_0(\boldsymbol{x}), \tag{5}$$

where $\overleftrightarrow{\boldsymbol{P}}_0 = c_s^2\rho\overleftrightarrow{\boldsymbol{I}}$ is the ideal-gas EOS. The nonideal force evaluation is thermodynamically consistent and Galilean invariant [12].

The above multiphase model is directly derived from thermodynamics; however, the evaluations of the pressure tensor and its divergence have high temporal and spatial complexity. Moreover, the pressure tensor cannot be conveniently used to express the wettability of a solid surface. Here, we introduce a chemical potential to evaluate the nonideal force. For a van der Waals (VDW) fluid, the chemical potential can be derived from the free-energy density function [19,24,28],

$$\mu = \frac{\partial\Phi}{\partial\rho} - \nabla\cdot\frac{\partial\Phi}{\partial(\nabla\rho)}, \tag{6}$$

where

$$\Phi(\rho) = \psi(\rho) + \frac{\kappa}{2}(\nabla\rho)^2. \tag{7}$$

Thus the chemical potential is computed by the density and free-energy density,

$$\mu = \psi'(\rho) - \kappa\nabla^2\rho. \tag{8}$$

From Eqs. (2) and (4), we find

$$P_{\alpha\beta} = \left[p_0 - \kappa\rho\nabla^2\rho - \frac{\kappa}{2}(\nabla\rho)^2\right]\delta_{\alpha\beta} + \kappa\frac{\partial\rho}{\partial x_\alpha}\frac{\partial\rho}{\partial x_\beta}. \tag{9}$$

Substituting Eq. (3) into Eq. (9), the divergence of the pressure tensor is written as

$$\frac{\partial}{\partial x_\beta}P_{\alpha\beta} = \frac{\partial}{\partial x_\alpha}\{\rho[\psi'(\rho) - \kappa\nabla^2\rho] - \psi(\rho)\} - \frac{\partial}{\partial x_\alpha}\left[\frac{\kappa}{2}(\nabla\rho)^2\right] + \kappa\frac{\partial}{\partial x_\beta}\left(\frac{\partial\rho}{\partial x_\alpha}\frac{\partial\rho}{\partial x_\beta}\right). \tag{10}$$

We take Eq. (8) and after some simple manipulations, a simple relationship between the divergence of the pressure tensor and the gradient of the chemical potential can be obtained:

$$\nabla\cdot\overleftrightarrow{\boldsymbol{P}} = \rho\nabla\mu. \tag{11}$$

Substituting Eq. (11) into Eq. (5), the nonideal force can be evaluated by the chemical potential in the form

$$\boldsymbol{F}(\boldsymbol{x}) = -\rho\nabla\mu + \nabla\cdot\overleftrightarrow{\boldsymbol{P}}_0(\boldsymbol{x}). \tag{12}$$

Then the nonideal force is incorporated into the lattice Boltzmann equation (LBE), which is fully discretized in space, time, and velocity. Several collision operators distinguish the variants of the LBE, such as the single-relaxation-time model [29–31], the multiple-relaxation-time model [32], the two-relaxation-time model [33], and the entropic lattice Boltzmann equation [34]. The single-relaxation-time version can be concisely written as

$$f_i(\boldsymbol{x}+\boldsymbol{e}_i, t+1) - f_i(\boldsymbol{x},t) = -\frac{1}{\tau}[f_i(\boldsymbol{x},t) - f_i^{(\mathrm{eq})}(\boldsymbol{x},t)], \tag{13}$$

where $f_i(\boldsymbol{x},t)$ is the particle distribution function at lattice site $\boldsymbol{x}$ and time t; $\boldsymbol{e}_i$ with $i = 0,\ldots,N$ is the discrete speed; τ the relaxation time; and $f_i^{(\mathrm{eq})}$ the equilibrium distribution function,

$$f_i^{(\mathrm{eq})}(\boldsymbol{x},t) = \rho\omega_i\left[1 + 3(\boldsymbol{e}_i\cdot\boldsymbol{u}) + \frac{9}{2}(\boldsymbol{e}_i\cdot\boldsymbol{u})^2 - \frac{3}{2}u^2\right], \tag{14}$$

where ω_i is the weighting coefficient and $\boldsymbol{u}$ the fluid velocity. The nonideal force acts on the collision process by increasing the particle momentum in the equilibrium distribution function, in which the fluid velocity is replaced by the equilibrium velocity $\boldsymbol{u}^{\mathrm{eq}} = \boldsymbol{u} + \tau\boldsymbol{F}/\rho$ [35]. Correspondingly, the macroscopic fluid velocity is redefined by the averaged momentum before and after the collision $\boldsymbol{v} = \boldsymbol{u} + \boldsymbol{F}/2\rho$.

In the above deductions, it is clear that no specific EOS is presupposed and Eq. (12) is established only if an EOS follows the form of Eq. (3) and the corresponding chemical potential meets the definition of Eq. (6). The model is then versatile to simulate various multiphase flows by adapting to its EOS, such as that of van der Waals (VDW), Redlich-Kwong, Peng-Robinson, and Carnahan-Starling. Equation (12) is mathematically equivalent to the previous version, namely, Eq. (5), based on the pressure tensor. Therefore, the nonideal force evaluation based on the chemical potential also theoretically satisfies thermodynamics and Galilean invariance. Furthermore, the chemical-potential-based model is efficient in both computing time and memory, because it avoids computing the pressure tensor and its divergence, which are computationally heavy and require more memory in the three-dimensional (3D) simulations of multiphase flows.

III. SPECIFIC CHEMICAL POTENTIALS

For a given equation of state p_0, solving Eq. (3), which is a typical one-order linear ordinary differential equation,

determinates the general solution of the free-energy density,

$$\psi = \rho\left(\int \frac{p_0}{\rho^2}d\rho + C\right), \tag{15}$$

where C is a constant, but it does not appear in the evaluation of the nonideal force below. Selecting several widely used EOSs, we solve their free-energy densities and chemical potentials.

The VDW EOS is the most famous cubic EOS,

$$p_0 = \frac{\rho RT}{1-b\rho} - a\rho^2, \tag{16}$$

where R is the universal gas constant, $-a$ the attraction parameter, and b the volume correction. The free-energy density and chemical potential are obtained by solving Eqs. (8) and (15),

$$\psi = \rho RT \ln\left(\frac{\rho}{1-b\rho}\right) - a\rho^2, \tag{17}$$

and

$$\mu = RT\left[\ln\left(\frac{\rho}{1-b\rho}\right) + \frac{1}{1-b\rho}\right] - 2a\rho - \kappa\nabla^2\rho. \tag{18}$$

The Redlich-Kwong (RK) EOS is generally more accurate than the VDW EOS by improving the attraction term,

$$p_0 = \frac{\rho RT}{1-b\rho} - \frac{a\alpha(T)\rho^2}{(1+b\rho)}, \tag{19}$$

where $\alpha(T) = 1/\sqrt{T}$. The Soave modification (RKS) involves a more complicated temperature function, $\alpha(T) = [1+(0.480+1.574\omega-0.176\omega^2)(1-\sqrt{T_r})]^2$, where ω is the acentric factor. Both equations share the same expression of free-energy density and chemical potential,

$$\psi^{\mathrm{RK}} = RT\rho\ln\frac{\rho}{1-b\rho} - \frac{a\alpha(T)}{b}\rho\ln(1+b\rho), \tag{20}$$

and

$$\mu^{\mathrm{RK}} = RT\ln\frac{\rho}{1-b\rho} + \frac{RT}{1-b\rho} - \frac{a\alpha(T)}{b}\ln(1+b\rho) - \frac{a\alpha(T)\rho}{1+b\rho} - \kappa\nabla^2\rho. \tag{21}$$

The Peng-Robinson (PR) EOS is often superior in predicting liquid densities,

$$p_0 = \frac{\rho RT}{1-b\rho} - \frac{a\alpha(T)\rho^2}{1+2b\rho-b^2\rho^2}, \tag{22}$$

where the temperature function is $\alpha(T) = [1+(0.37464+1.54226\omega-0.26992\omega^2)(1-\sqrt{T/T_c})]^2$. Its free-energy density and chemical potential are

$$\psi^{\mathrm{PR}} = RT\rho\ln\frac{\rho}{1-b\rho} - \frac{a\alpha\rho}{2\sqrt{2}b}\ln\frac{\sqrt{2}-1+b\rho}{\sqrt{2}+1-b\rho}, \tag{23}$$

and

$$\mu^{\mathrm{PR}} = RT\ln\frac{\rho}{1-b\rho} - \frac{a\alpha(T)}{2\sqrt{2}b}\ln\frac{\sqrt{2}-1+b\rho}{\sqrt{2}+1-b\rho} + \frac{RT}{1-b\rho} - \frac{a\alpha(T)\rho}{1+2b\rho-b^2\rho^2} - \kappa\nabla^2\rho. \tag{24}$$

The Carnahan-Starling (CS) EOS tends to give better approximations for the repulsive term,

$$p_0 = \rho RT\frac{1+b\rho/4+(b\rho/4)^2-(b\rho/4)^3}{(1-b\rho/4)^3} - a\rho^2, \tag{25}$$

for which the free-energy density and chemical potential are

$$\psi^{\mathrm{CS}} = RT\rho\left[\frac{3-b\rho/2}{(1-b\rho/4)^2} + \ln\rho\right] - a\rho^2, \tag{26}$$

and

$$\mu^{\mathrm{CS}} = RT\left[\frac{3-b\rho/4}{(1-b\rho/4)^3} + \ln\rho + 1\right] - 2a\rho - \kappa\nabla^2\rho. \tag{27}$$

In the following simulations, the attraction parameter and the volume correction take $a = 2/49$, $b = 2/21$ for PR and RKS EOS and $a = 1$, $b = 4$ for CS EOS. The universal gas constant is $R = 1$. The acentric factor ω is 0.344 for water and 0.011 for methane. In an effort to relate the numerical results to the real physical properties, we define the reduced variables $T_r = T/T_c$ and $\rho_r = \rho/\rho_c$, where T_c is the critical temperature and ρ_c the critical density.

IV. CHEMICAL-POTENTIAL BOUNDARY CONDITION

Chemical potential, which has a clear physical meaning, is a more effective way to express the wettability of a solid surface than density or effective mass (i.e., pseudopotential) [8,9,36,37]. An external chemical potential was once used at the surfaces of a confined system to study wetting [16]. In the present study, since the multiphase model is driven by a chemical potential, the implementation of the chemical-potential boundary condition is simple and quite natural. Endowing a solid surface with a specific chemical potential, the wettability, namely, the interaction between the fluid and the solid, can be easily expressed.

Let us locate the straight interface of fluid and solid on a row of lattice nodes ($y = 1$), which are treated as fluid nodes. The distribution functions on these interfacial fluid nodes still collide and stream. The bounceback boundary condition is applied to mimic those distribution functions from the solid. The solid nodes ($y = 0$) are assigned a specific chemical potential, which indicates the wetting property of the solid surface. It influences the nonideal force on the interfacial fluid nodes by Eq. (12) and then reflects the interaction between fluid and the solid surface. Since the chemical potential on the solid nodes is specified, the formula of chemical potential, namely, Eq. (8), will never calculate on the solid nodes.

In order to evaluate the density gradient in Eq. (12) on the interfacial fluid nodes ($y = 1$), we need to estimate the densities on the lattice nodes ($y = 0$). A simple weighted average scheme [38] based on the neighbor fluid nodes is applied,

$$\rho(x,\,0) = \tfrac{2}{3}\rho(x,\,1) + \tfrac{1}{6}\rho(x-1,\,1) + \tfrac{1}{6}\rho(x+1,\,1), \tag{28}$$

where $\rho(x,y)$ is the density at the lattice node (x,y).

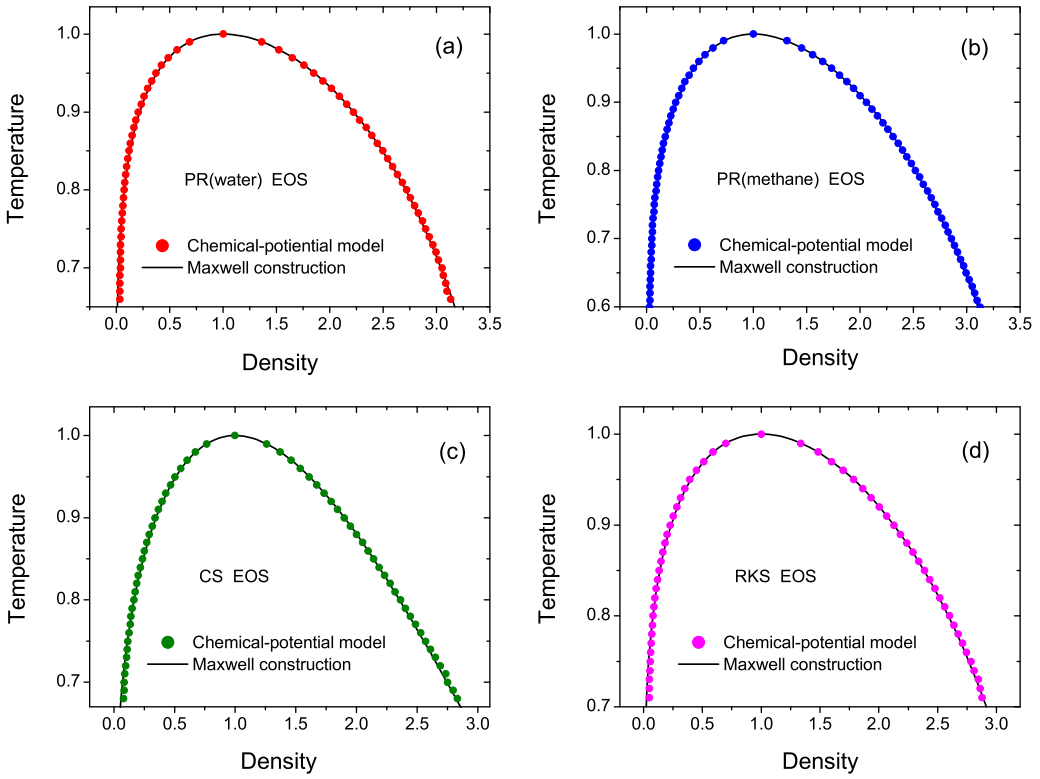

FIG. 1. Two-phase coexistence density curves of (a) PR for water, (b) PR for methane, (c) CS and (d) RKS EOSs compared with the theoretical predictions solved by the Maxwell equal-area construction.

V. SIMULATION AND VERIFICATION

We now present a series of numerical simulations, in which first-order phase transitions occur, to demonstrate the qualities of the chemical-potential-based multiphase flow model. To evaluate the nonideal force, we firstly compute the chemical potential at every lattice node and then the gradient. The weighted average central difference scheme [38] is used to compute the gradients of the density and the chemical potential.

A. Two-phase coexistence density

The two-phase coexistence densities solved by the Maxwell equal-area construction are used as benchmarks to verify the thermodynamic consistency of the present model. The computational domain is a rectangular with the periodical boundary condition. The length is 100 and the width is 200 lattice units. With horizontal phase interfaces, the middle part of the domain is initialized as liquid, while the remaining part is set as gas. The relaxation time is 1.3 and the value of κ in Eq. (8) is 0.01. Four EOSs, namely CS, RKS, and PR for water and methane, are evaluated and compared with the theoretical predictions. From Fig. 1, the present numerical simulations are all in excellent agreement with the benchmarks. This supports that the present model is thermodynamically consistent. The liquid to gas density ratios computed by PR EOS for water and methane are more than 100. Only if a proper EOS is chosen, the present model is competent to accurately simulate real physical systems.

B. Two-drop coalescence

The drop coalescence is simulated with the different reference frames to show Galilean invariance of the present multiphase model. The computational domain is a square with side length 500 lattice units. The temperature is $T_r = 0.85$. The drop radius is 50 lattice units and the interval between the two drops is 12 lattice units. Four reference frames are

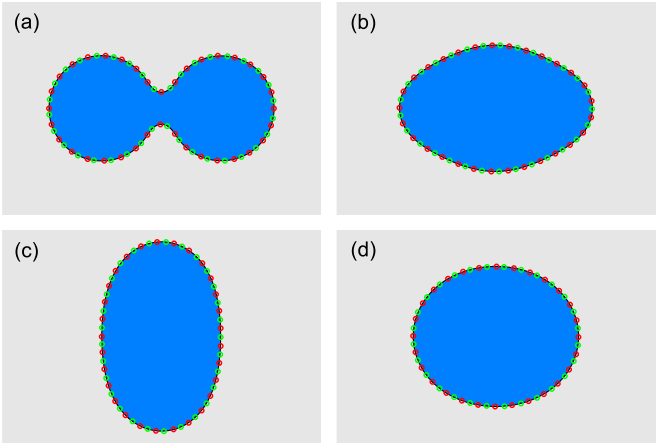

FIG. 2. Drop coalescence with the different reference frames at (a) $t = 1500$, (b) $t = 3500$, (c) $t = 6000$, and (d) $t = 10000$ time steps. The blue contours have a static reference frame, while the reference frame velocities are 0.02 for the black lines, the red circles and the green circles with the angles 0°,23°,45°, respectively.

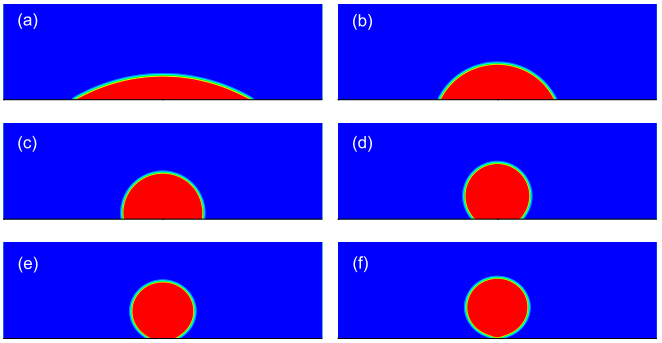

FIG. 3. Contact angles obtained on solid surfaces with different chemical potentials by using RKS EOS: (a) $\theta = 30^\circ$ at $\mu = -0.23$, (b) $\theta = 60^\circ$ at $\mu = -0.13$, (c) $\theta = 105^\circ$ at $\mu = 0$, (d) $\theta = 135^\circ$ at $\mu = 0.09$, (e) $\theta = 160^\circ$ at $\mu = 0.15$, (f) $\theta = 180^\circ$ at $\mu = 0.18$.

applied in the simulations. The blue contours have a static reference frame. The black lines, the red circles, and the green circles have moving reference frames with the velocity 0.02 and the angles 0°, 23°, 45°, respectively. Figure 2 illustrates four typical geometries at 1500, 3500, 6000, and 10000 time steps in the coalescence process. The excellent agreements show that the present model satisfies Galilean invariance in the dynamic drop coalescence.

C. Linear-tunable contact angle

Contact angle is an essential feature to reflect the wettability of a solid surface. In this section, we illustrate how the chemical-potential-based model can effectively simulate the wetting phenomena. The computational domain is rectangular with the length 500 and the width 200 lattice units. The left and right sides are the periodical boundary condition while the top and bottom sides are the chemical-potential boundary condition. The drop radius is 50 lattice units. For the top side, the value of chemical potential is optional because the drop never touches it. Typically, the chemical potential on the top side takes the same value as that in its neighboring fluid node, which is always gas phase in the simulations. Without gravity, a droplet on a horizontal solid surface forms a perfect spherical cap. If the base and height of the droplet are L and H, the radius of the droplet is calculated by $R = (4H^2 + L^2)/8H$ and then the contact angle is obtained by the formula $\tan\theta = L/2(R - H)$.

To illustrate the wettability of different surfaces, a sessile drop on a solid surface with specified chemical potentials is simulated using the RKS EOS. Figure 3 demonstrates that the present model can effectively simulate a drop on the solid surfaces from hydrophilic to superhydrophobic.

The relationship between the chemical potential and the contact angle is further investigated. The numerical simulations include four equations of state, namely, RKS EOS, CS EOS, and the PR EOSs for both water and methane. As shown in Fig. 4, with the growth of the chemical potential of the solid surface, the simulating contact angles smoothly increase. Remarkably, the contact angle increases almost linearly with increasing chemical potential. A linear-tunable contact angle is very convenient to adjust the wettability of the solid surface in numerical simulations.

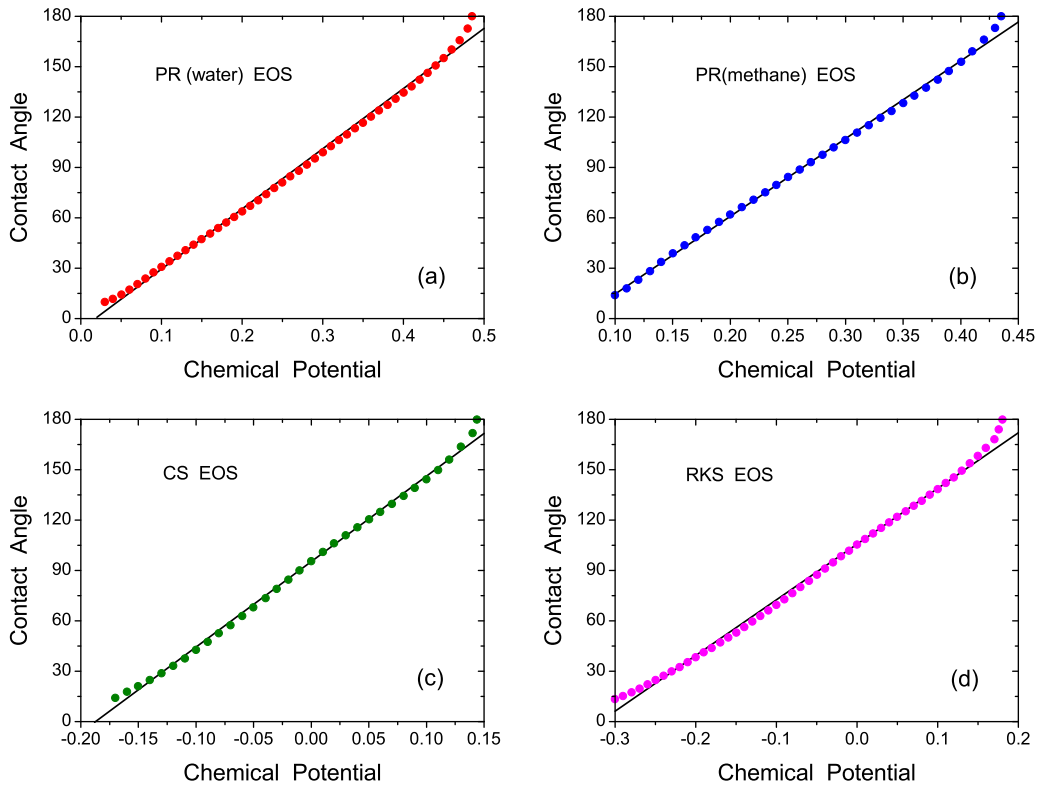

FIG. 4. Contact angle increasing with the chemical potential of the solid surface at the reduced temperature 0.8, (a) PR for water, (b) PR for methane, (c) CS, and (d) RKS EOSs.

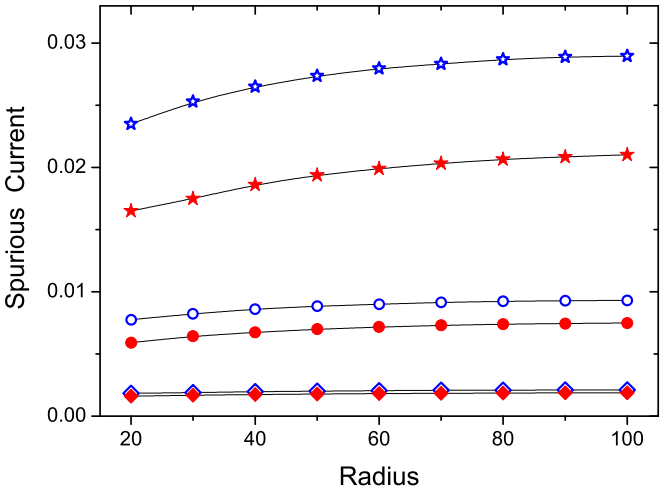

FIG. 5. The spurious currents of a rest drop surrounded by gas. The red solid symbols ★, ●, and ◆ represent the spurious currents on the present model with the temperatures 0.80, 0.85, and 0.90, respectively. The blue hollow symbols ◇, ○, and ☆ represent the spurious currents on the pressure-tensor-based model with the temperatures 0.80, 0.85, and 0.90, respectively.

D. Spurious current

Without gravity, a liquid drop surrounded by gas phase is simulated to compare the spurious currents of the present model and the pressure-tensor-based version [12]. When the system reaches its mechanical equilibrium state, the level of spurious currents is represented by the largest macroscopic velocity in the flow field. The system is simulated at the temperatures 0.80, 0.85, and 0.90, while the drop radius changes from 20 to 100 lattice units. Figure 5 shows that the lower temperature leads to higher spurious currents. The spurious currents in the present model (red symbols) are clearly lower than that in the pressure-tensor-based model (blue symbols). This indicates that although the chemical-potential-based model is mathematically equivalent to the pressure-tensor-based model, there are still some differences between the theoretical analysis and the numerical simulation [24].

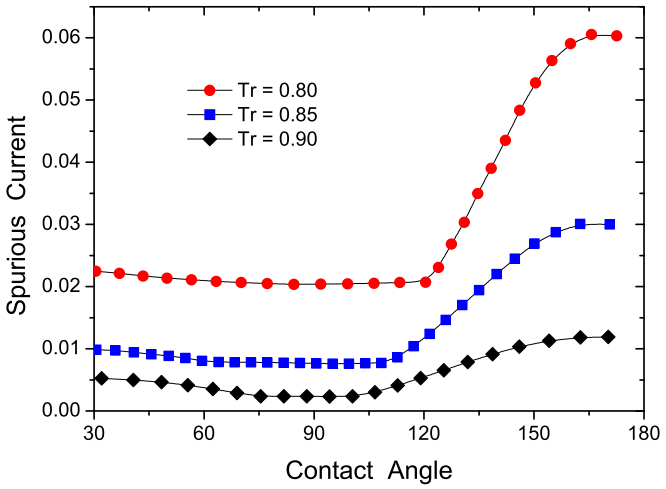

FIG. 6. The spurious currents of a sessile drop on the horizontal surfaces with different wettability at the temperatures 0.80, 0.85, and 0.90.

TABLE I. The largest ten spurious currents in the left and right three-phase contact regions of the drop.

	Left three phase contact region		Right three phase contact region	
No.	Lattice node	Spurious current	Lattice node	Spurious current
1	(222, 1)	0.05548	(278, 1)	0.05548
2	(221, 1)	0.05154	(279, 1)	0.05154
3	(223, 1)	0.05126	(277, 1)	0.05126
4	(220, 1)	0.04215	(280, 1)	0.04215
5	(224, 1)	0.04166	(276, 1)	0.04166
6	(219, 1)	0.03145	(281, 1)	0.03145
7	(225, 1)	0.03142	(275, 1)	0.03142
8	(221, 2)	0.02765	(279, 2)	0.02765
9	(222, 2)	0.02667	(278, 2)	0.02667
10	(220, 2)	0.02421	(280, 2)	0.02421

The spurious currents are further investigated in the simulations of a sessile drop on solid surfaces with different contact angles. The computational domain is rectangular with the length 500 and the width 200 lattice units. The drop radius is 50 lattice units. The chemical-potential boundary condition is used for the bottom boundary. Figure 6 shows the spurious currents in the simulations of the contact angles from 30° to 170° at the temperature 0.80, 0.85, and 0.90. In the left part (hydrophilic surface), the spurious currents are slightly higher than those in Fig. 6. However, in the right part (hydrophobic surface), the spurious currents rise remarkably, especially at the temperature 0.80.

Table I contains the lattice nodes with the largest 20 spurious currents in the simulation with the contact angle 150° at the temperature 0.80. As expected, the nodes with the large spurious currents locate in the left and right three-phase contact regions. It is clear that the spurious currents have symmetrical distributions in the two regions. The remarkable increases of spurious currents (more than 0.03) are only on seven nodes in each region and are all on the interface fluid nodes ($y = 1$). In the rest of the parts of the flow field, the spurious currents are similar to the borderless cases.

VI. CONCLUSION

We performed a multiphase lattice Boltzmann model for nonideal fluid based on chemical potential. The model is mathematically equivalent to the previous pressure-tensor-based multiphase model, which theoretically satisfies thermodynamics and Galilean invariance. A graceful relationship between the divergence of the pressure tensor and the gradient of the chemical potential has been obtained. The calculations of the pressure tensor and its divergence in the pressure-tensor-based model are avoided and thereby the computational efficiency is also improved. The model is versatile in simulating various multiphase flows by cooperating with different EOSs. Several chemical potentials of the popular equations of state have been

derived. The theoretical analyses and numerical results support that the present model satisfies thermodynamics and Galilean invariance. The present model produces lower spurious currents than the pressure-tensor-based model. This indicates that although they are mathematically equivalent, there are some numerical differences between them. To investigate the surface wettability, a chemical-potential boundary condition was implemented to effectively simulate the wetting of solid surfaces from hydrophilic to superhydrophobic. The contact angle can be linearly tuned by the chemical potential of the solid surface. The present method is expected to promote the studies of multiphase flows in real physical systems.

ACKNOWLEDGMENTS

This work was supported by the National Natural Science Foundation of China (Grants No. 11362003, No. 11462003, No. 11290164, and No. 11162002), Guangxi Natural Science Foundation (Grant No. 2014GXNSFAA118018), Guangxi Science and Technology Foundation of College and University (Grant No. KY2015ZD017), Guangxi "Bagui Scholar" Teams for Innovation and Research Project, Guangxi Collaborative Innovation Center of Multi-source Information Integration and Intelligent Processing, CAS-Shanghai Science Research Center (Grant No. CAS-SSRC-YJ-2015-01).

[1] S. Chen and G. Doolen, Annu. Rev. Fluid Mech. **30**, 329 (1998).
[2] C. Aidun and J. Clausen, Annu. Rev. Fluid Mech. **42**, 439 (2010).
[3] Q. Li, K. H. Luo, Q. J. Kang, Y. L. He, Q. Chen, and Q. Liu, Prog. Energy Combust. Sci. **52**, 62 (2016).
[4] L. Chen, Q. Kang, Y. Mu, Y.-L. He, and W.-Q. Tao, Int. J. Heat Mass Transfer **76**, 210 (2014).
[5] A. Ladd and R. Verberg, J. Stat. Phys. **104**, 1191 (2001).
[6] B. Wen, C. Zhang, Y. Tu, C. Wang, and H. Fang, J. Comput. Phys. **266**, 161 (2014).
[7] B. Wen, C. Zhang, and H. Fang, Entropy **17**, 27 (2015).
[8] X. Shan and H. Chen, Phys. Rev. E **47**, 1815 (1993).
[9] R. Benzi, L. Biferale, M. Sbragaglia, S. Succi, and F. Toschi, Phys. Rev. E **74**, 021509 (2006).
[10] P. Yuan and L. Schaefer, Phys. Fluids **18**, 042101 (2006).
[11] Q. Li, K. H. Luo, and X. J. Li, Phys. Rev. E **86**, 016709 (2012).
[12] B. Wen, Z. Qin, C. Zhang, and H. Fang, Europhys. Lett. **112**, 44002 (2015).
[13] S. Khajepor, J. Wen, and B. Chen, Phys. Rev. E **91**, 023301 (2015).
[14] G. Falcucci, S. Ubertini, and S. Succi, Soft Matter **6**, 4357 (2010).
[15] A. Montessori, G. Falcucci, M. La Rocca, S. Ansumali, and S. Succi, J. Stat. Phys. **161**, 1404 (2015).
[16] M. R. Swift, W. R. Osborn, and J. M. Yeomans, Phys. Rev. Lett. **75**, 830 (1995).
[17] T. Inamuro, N. Konishi, and F. Ogino, Comput. Phys. Commun. **129**, 32 (2000).
[18] T. Inamuro, T. Ogata, S. Tajima, and N. Konishi, J. Comput. Phys. **198**, 628 (2004).
[19] H. W. Zheng, C. Shu, and Y. T. Chew, J. Comput. Phys. **218**, 353 (2006).
[20] J. Y. Shao, C. Shu, H. B. Huang, and Y. T. Chew, Phys. Rev. E **89**, 033309 (2014).
[21] Y. Wang, C. Shu, J. Y. Shao, J. Wu, and X. D. Niu, J. Comput. Phys. **290**, 336 (2015).
[22] Y. Wang, C. Shu, H. B. Huang, and C. J. Teo, J. Comput. Phys. **280**, 404 (2015).
[23] A. Mazloomi M, S. S. Chikatamarla, and I. V. Karlin, Phys. Rev. Lett. **114**, 174502 (2015).
[24] D. Jamet, D. Torres, and J. U. Brackbill, J. Comput. Phys. **182**, 262 (2002).
[25] Y. Y. Yan and Y. Q. Zu, J. Comput. Phys. **227**, 763 (2007).
[26] S. R. De Groot and P. Mazur, *Nonequilibrium Thermodynamics* (North-Holland, Amsterdam, 1962).
[27] R. F. Cracknell, D. Nicholson, and N. Quirke, Phys. Rev. Lett. **74**, 2463 (1995).
[28] J. S. Rowlinson and B. Widom, *Molecular Theory of Capillarity* (Clarendon, Oxford, 1982).
[29] S. Y. Chen, H. D. Chen, D. Martinez, and W. Matthaeus, Phys. Rev. Lett. **67**, 3776 (1991).
[30] H. D. Chen, S. Y. Chen, and W. H. Matthaeus, Phys. Rev. A **45**, R5339(R) (1992).
[31] Y. H. Qian, D. d'Humières, and P. Lallemand, Europhys. Lett. **17**, 479 (1992).
[32] P. Lallemand and L. S. Luo, Phys. Rev. E **61**, 6546 (2000).
[33] I. Ginzburg, F. Verhaeghe, and D. d'Humières, Commun. Comput. Phys. **3**, 427 (2008).
[34] I. V. Karlin, A. Ferrante, and H. C. Ottinger, Europhys. Lett. **47**, 182 (1999).
[35] X. Shan and G. Doolen, J. Stat. Phys. **81**, 379 (1995).
[36] N. S. Martys and H. Chen, Phys. Rev. E **53**, 743 (1996).
[37] Q. Li, K. H. Luo, Q. J. Kang, and Q. Chen, Phys. Rev. E **90**, 053301 (2014).
[38] T. Lee and C.-L. Lin, J. Comput. Phys. **206**, 16 (2005).